Mechanism of membrane fusion induced by vesicular stomatitis virus G protein

Irene S. Kim[a,1], Simon Jenni[a], Megan L. Stanifer[b,2], Eatai Roth[c], Sean P. J. Whelan[b], Antoine M. van Oijen[a,3], and Stephen C. Harrison[a,d,4]

[a]Department of Biological Chemistry and Molecular Pharmacology, Harvard Medical School, Boston, MA 02115; [b]Department of Microbiology and Immunobiology, Harvard Medical School, Boston, MA 02115; [c]Department of Biology, University of Washington, Seattle, WA 98195; and [d]Howard Hughes Medical Institute, Harvard Medical School and Boston Children's Hospital, Boston, MA 02115

Contributed by Stephen C. Harrison, November 17, 2016 (sent for review October 10, 2016; reviewed by Axel T. Brunger and Frederick M. Hughson)

The glycoproteins (G proteins) of vesicular stomatitis virus (VSV) and related rhabdoviruses (e.g., rabies virus) mediate both cell attachment and membrane fusion. The reversibility of their fusogenic conformational transitions differentiates them from many other low-pH-induced viral fusion proteins. We report single-virion fusion experiments, using methods developed in previous publications to probe fusion of influenza and West Nile viruses. We show that a three-stage model fits VSV single-particle fusion kinetics: (*i*) reversible, pH-dependent, G-protein conformational change from the known prefusion conformation to an extended, monomeric intermediate; (*ii*) reversible trimerization and clustering of the G-protein fusion loops, leading to an extended intermediate that inserts the fusion loops into the target-cell membrane; and (*iii*) folding back of a cluster of extended trimers into their postfusion conformations, bringing together the viral and cellular membranes. From simulations of the kinetic data, we conclude that the critical number of G-protein trimers required to overcome membrane resistance is 3 to 5, within a contact zone between the virus and the target membrane of 30 to 50 trimers. This sequence of conformational events is similar to those shown to describe fusion by influenza virus hemagglutinin (a "class I" fusogen) and West Nile virus envelope protein ("class II"). Our study of VSV now extends this description to "class III" viral fusion proteins, showing that reversibility of the low-pH-induced transition and architectural differences in the fusion proteins themselves do not change the basic mechanism by which they catalyze membrane fusion.

membrane fusion protein | virus entry | enveloped virus

Enveloped viruses initiate infection by fusion of the viral membrane with a membrane of the presumptive host cell. Conformational changes in surface-expressed, membrane-anchored "fusion proteins," coupled with attachment to the target membrane, overcome the kinetic barrier to bilayer merger (1, 2). A general model for these fusion-inducing conformational changes, derived from studies of many viral fusion proteins, invokes a canonical sequence of events: a priming step, often a proteolytic cleavage and usually irreversible; a triggering step, such as exposure to low pH in endosomes or, for some viruses, receptor binding; formation of an extended intermediate, from which hydrophobic fusion loops or fusion peptides insert into the target membrane; and collapse of that intermediate to a final, stable conformation that brings together the fusion loops or peptides and the transmembrane anchor, and hence pulls together the two membranes (3). Structures of the initial (prefusion) conformation, both unprimed and primed, and the final (postfusion) conformation have shown the beginning and end of the fusion process for many enveloped viruses (4); studies of single virus–particle fusion kinetics have probed the intervening stages in some detail for influenza and West Nile viruses (5–7).

The fusion glycoprotein (G protein) of vesicular stomatitis virus (VSV) and related rhabdoviruses (e.g., rabies virus) is the sole surface-expressed protein on the bullet-shaped virions. It mediates both attachment and low-pH-induced fusion (8). Its fusogenic conformational changes deviate from the canonical sequence outlined in the preceding paragraph by the absence of an irreversible priming step and hence the absence of a metastable prefusion state. The transition from prefusion conformation to extended intermediate is reversible (9, 10). Nonetheless, structures of G in its pre- and postfusion trimeric conformations suggest that most of the fusion reaction follows a familiar pattern, as illustrated in Fig. 1 (3, 11–13). We show the extended intermediate as a monomer, because the two structures appear to require a dissociative transition from pre- to postfusion trimer (Fig. 1, open and extended conformations). Note that in this inferred picture of the transition from prefusion to postfusion conformations, the exposed lateral surfaces of the apical domain of the molecule (those facing left and right in the first panel of Fig. 1) become buried along the threefold contact when the extended intermediate trimerizes and that the extended C-terminal segment "zips" up along the outside of this trimer during the fold-back step.

We report here single-virion fusion experiments, carried out on VSV. Fusion of two lipid bilayers generally proceeds through a hemifusion state, in which the apposed leaflets have merged but not the distal leaflets (6); we can detect hemifusion by observing transfer of a fluorescent molecule from one membrane to the other. In particular, we have inserted a lipophilic dye, R18,

Significance

Enveloped viruses—those with a lipid-bilayer membrane such as influenza, dengue, and human immunodeficiency viruses—enter cells by fusion of the viral membrane with a membrane of the cell. A viral surface glycoprotein, known as its "fusion protein," facilitates this step. Previous work studying the kinetics of single virus particles fusing with a target membrane has outlined a mechanism by which conformational changes in the fusion protein accelerate merger of the two bilayers. In this paper, we extend that mechanism to a structurally distinct class of viral fusion proteins, providing strong evidence for its general applicability to all viral membrane fusion processes.

Author contributions: I.S.K., S.P.J.W., A.M.v.O., and S.C.H. designed research; I.S.K. acquired data; I.S.K., A.M.v.O., and S.C.H. analyzed data; I.S.K. and S.J. designed and implemented the kinetic model; M.L.S. and S.P.J.W. contributed new reagents; E.R. contributed new analytic tools; and I.S.K., S.J., and S.C.H. wrote the paper.

Reviewers: A.T.B., Stanford University; and F.M.H., Princeton University.

The authors declare no conflict of interest.

Freely available online through the PNAS open access option.

[1]Present address: Division of Biology and Biological Engineering, California Institute of Technology, Pasadena, CA 91125.

[2]Present address: Department of Infectious Diseases, Virology, Heidelberg University, D-6920 Heidelberg, Germany.

[3]Present address: School of Chemistry, University of Wollongong, Wollongong, NSW 2522, Australia.

[4]To whom correspondence should be addressed. Email: harrison@crystal.harvard.edu.

This article contains supporting information online at www.pnas.org/lookup/suppl/doi:10.1073/pnas.1618883114/-/DCSupplemental.

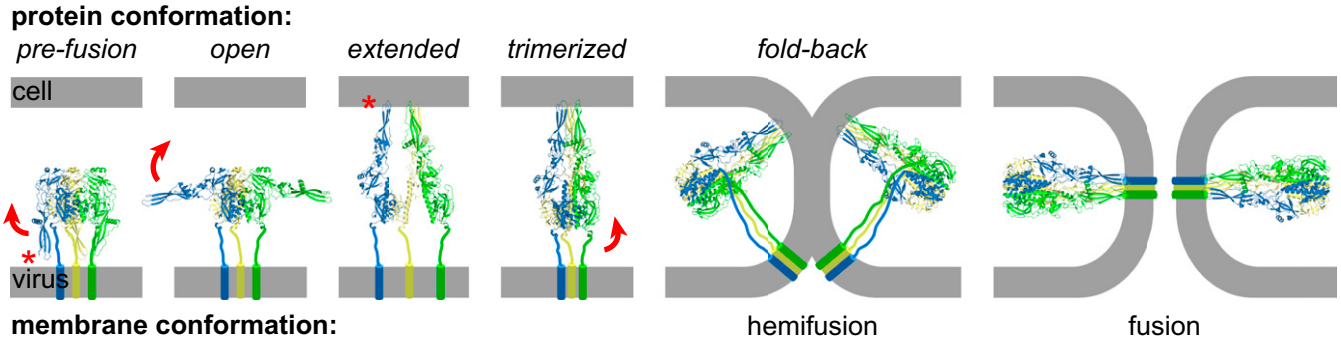

Fig. 1. Proposed pathway of sequential conformational changes in G that drive membrane fusion. G is a trimer in both its prefusion and postfusion states. The G monomers are colored blue, green, and yellow, respectively. C-terminal ectodomain residues missing from the crystal structures are drawn as thick lines; transmembrane residues, as rods. The lipid bilayers are drawn as gray bars; the viral membranes are along the bottom of the figure, and the cell membranes, along the top. The fusion loops on one monomer are indicated by a red asterisk (33). "Open": the proposed open conformation (G*) results from protonation of each G monomer, leading to swinging out of the "arms" composed of domains 3 and 4 (21, 34). "Extended": Subsequent rotation between the PH (pleckstrin homology) domain and these arms and a loop-to-helix transition in the PH domain direct the fusion loops toward the cell membrane; these conformational changes disrupt the prefusion trimer interfaces. "Trimerized": Trimerization of three adjacent monomers in extended conformation. "Fold-back": Zipping-up of the C-terminal residues along the outside of the trimer draws the cell and viral membranes together, leading to hemifusion. Formation of the final postfusion conformation drives pore formation and complete membrane fusion. Prefusion (*Left*) and postfusion(*Right*) trimer models are from known crystal structures [Protein Data Bank (PDB) codes 5I2S (12) and 5I2M (11), respectively].

into the viral membrane at self-quenching concentrations and recorded the time elapsed between a fusion-inducing pH drop and dequenching of the fluorophore followed by dissipation of its fluorescent signal by diffusion in the target membrane. We find that the kinetic data are indeed consistent with the general picture shown in Fig. 1. By varying both initial and final pH, we can separate the kinetic steps and show that the following three-stage model fits the observations. The first step is a reversible, pH-dependent G-protein conformational change, corresponding to the transition from "prefusion" to "extended" in Fig. 1; the second, a reversible G trimerization and clustering of fusion loops ("extended" to "trimerized"); and the third, folding back to bring together the two membranes. The membranes resist this collapse, and a critical number of adjacent, extended trimers spanning the contact zone between virus and target membrane are necessary to progress forward to hemifusion. Computational simulations match the observations if the critical cluster is chosen as 3, 4, or 5 trimers, within a contact zone of 30 to 50 G trimers. The time required to accumulate this critical cluster determines the overall rate of the fusion reaction. This mechanism is essentially the same as the ones previously described for influenza and West Nile viruses (5–7), despite differences in the structures of their fusion proteins, which represent each of the three "classes" so far described (3).

Results

pH Dependence of VSV Hemifusion. We used total internal reflection fluorescence (TIRF) microscopy, in a configuration similar to the one described previously (Fig. 2 *A* and *B*) (6), to follow single-particle VSV fusion with a supported lipid bilayer under nine different regimes of initial and final pH (Fig. 2 *C*–*F*). We labeled the VSV membrane with quenching concentrations of a lipophilic dye, R18. The virus attached to the bilayer at the initial pH; a rapid pH drop initiated the fusogenic conformational change in G. At the time of hemifusion, R18 could diffuse from the viral membrane into the target bilayer, leading to dequenching of the R18 signal and then rapid dissipation (Fig. 2*B* and Movie S1). For each experiment, the initial pH was higher than that of the fusion threshold (pH 6.4) (14). The mean time from pH drop (detected by the pH-dependent loss of fluorescence from the fluorescein incorporated into the membrane) to hemifusion (detected by R18 dequenching) depended on both initial and final pH (Fig. 2*C*); it decreased as either limiting pH decreased. At the lowest final pH (5.5), the mean time to hemifusion approached 25 to 30 s, regardless of the initial pH.

At high initial or final pH, the hemifusion frequency distributions showed a rise and decay, the signature of more than one rate-limiting step (Fig. 2 *D* and *E*, *Top*). As the final pH decreased, the distribution shifted to an exponential decay (Fig. 2 *D–F*, *Bottom*), the characteristic distribution for a single rate-limiting step. A similar trend applied to the initial pH (Fig. 2 *D–F*, *Top*) but, even at pH 6.6, the shape of the distribution was not a simple exponential.

pH Dependence of VSV–Membrane Association. During the hemifusion experiments, we observed that the VSV particle attached to the membrane in two modes. In a "rolling" mode, the virions moved along the bilayer in the direction of flow, while clearly maintaining contact with the bilayer, as they remained within the TIRF evanescent field (Fig. 3*A*, particle 1). In an "arrested" mode, virions were immobile, even if subject to drag in the flow cell of the microscope (Fig. 3*A*, particles 2 and 3; see also Movie S2). Both rolling and arrested virions underwent hemifusion following the drop in pH. Rolling virions arrested rapidly during the short (2- to 4-s) period that marked the transition from initial to final pH, and all particles had arrested by the time, t_0, at which the pH in the flow cell had dropped to its final level. When the initial pH was 6.6, all virions were arrested, even before the pH drop. Because pH 6.6 is also the point at which a single, rate-limiting step determines the hemifusion time distribution and other steps become much faster, this result suggests that the molecular transitions responsible for virion rolling and arrest are related to the pH-dependent steps in VSV hemifusion.

Fig. 3*B* shows a more detailed analysis of the pH dependence of rolling. Virions bound to the target bilayer were equilibrated for 5 to 10 min at one pH and then imaged under flow at that same pH. The percentage of rolling virions decreased roughly linearly with pH (Fig. 3*B*). At pH 8.0, over 60% of the bound virions were moving; at pH 7.4, about 30%; at pH 6.6, virtually all bound virions were stationary, consistent with our observations in the pH-drop experiments. The mean speed of the rolling population of virions also decreased steadily with pH (Fig. 3*C*).

The transition between rolling and arrest is reversible. When we raised the pH from 6.6, at which all virions were stationary, to 7.4, many of the arrested virions began to roll. When the pH was

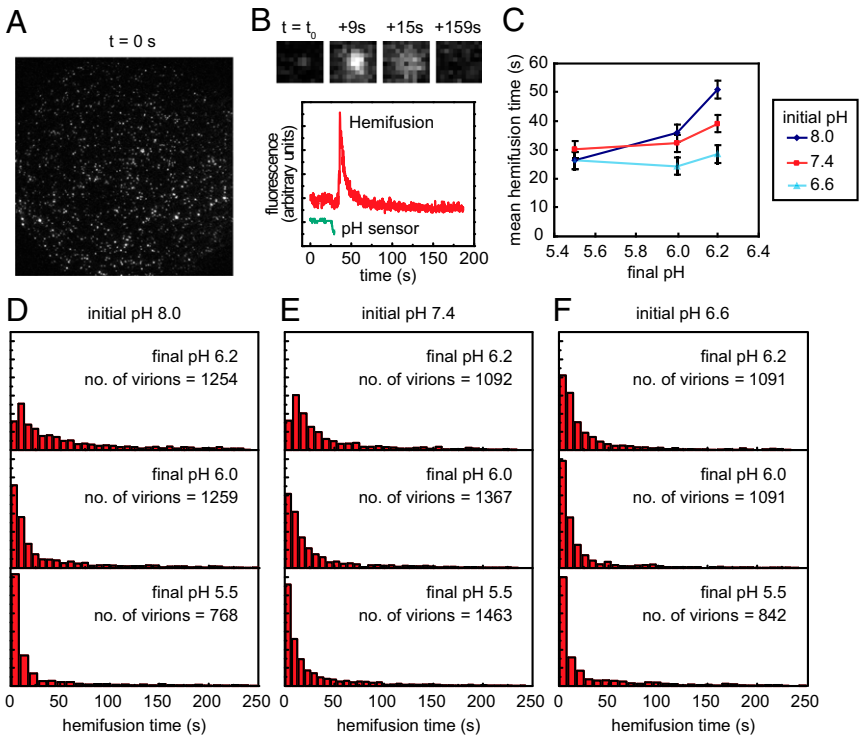

Fig. 2. Hemifusion kinetics of VSV. (*A*) Representative TIRF image of labeled virus particles bound to a lipid bilayer. Virus particles, whose membranes are labeled with fluorescent lipophilic dye R18, enter the flow-cell channel and bind nonspecifically to a target lipid bilayer, supported on a glass coverslip. Fluoresceinated lipid in the bilayer acts as an internal pH sensor, as the fluorescence yield of fluorescein decreases with pH. Introduction of low-pH buffer triggers hemifusion. (*B*) Snapshots of a single hemifusing virus particle (*Top*) and corresponding intensity traces (*Bottom*). The fluorescein intensity trace is in green; the R18 intensity trace, in red; t_0 is the time at which low pH is detected in the flow cell by loss of fluorescein intensity. Hemifusion is detected by a sharp rise in intensity due to dequenching of the lipophilic R18 dye upon lipid mixing. (*C*) Mean hemifusion times measured at different initial and final pH values. VSV particles bound to the target bilayer were incubated at one of three initial pH values (legend). The pH was then lowered to one of three final values (*x* axis) to initiate hemifusion. The mean hemifusion times were calculated from the hemifusion time distributions shown in *D*–*F*. Error bars show standard deviation (SD). (*D*–*F*) Distributions of hemifusion times measured at varied initial and final pH values. Initial pH at the top of each figure; final pH, within each plot. Each vertical bind represents the fraction of the VSV population that has hemifused within the time interval indicated on the *x* axis. The number of bins in each histogram does not exceed the square root of the number of virions in each distribution. The heights of the bins have been normalized such that the area under the curve equals one.

lowered again to 6.6, the rolling stopped (Fig. 3*D*). We interpret this observation by assuming a reversible, pH-dependent transition from the prefusion conformation, in which the fusion loops of G project back toward the viral membrane around the periphery of the trimer (Fig. 1, prefusion conformation), to an extensible monomer, in which the fusion loops can contact the target membrane (Fig. 1, extended conformation). Because we did not use a surrogate receptor in our experiments [such as the equivalent of a ganglioside in work on influenza virus fusion (6, 7) or a lectin domain in studies of West Nile virus fusion (5)], attachment to the supported bilayer was probably through reversible exposure of the fusion loops, even at pH 8.0. As the pH dropped, the equilibrium shifted toward loop exposure, and more extensive interactions anchored the particle firmly enough to resist solvent drag. Reversibility of the rolling phenomenon indicates that membrane interaction of extended G at pH ≥6.6 is itself reversible.

pH Transitions and Conformation of VSV G. The pH dependence of virion binding derives from conformational changes in the surface-expressed G protein. We examined changes in the G-protein layer by negative-stain electron microscopy of VSV particles incubated at pH 7.6, 7.0, and 6.6 (Fig. S1). As previously reported (15), the G layer at pH 7.6 was shallow (average depth 6.0 ± 0.4 nm) and appeared indistinct (Fig. S1*A*), whereas at pH 6.6, most of the G layer was deeper (average depth 10.5 ± 0.6 nm) and appeared more ordered (Fig. S1*C*). At pH 7.0, patches of the longer form of G appeared interspersed with patches of the shorter form of G (Fig. S1*B*). These observations suggest that as the pH decreases from 7.6 to 6.6, the G layer of the particle gradually converts from the short form to the long form.

We used a liposome-binding experiment to estimate the pK_a of the transition of G into a membrane-interacting conformation. We generated the G ectodomain (G_{th}) by thermolysin cleavage of intact virus particles and purified it by anion-exchange chromatography. We also made G_{th} from a fusion-loop mutant, G-W72A, which substitutes alanine for a conserved, fusion-loop tryptophan (Fig. 4*A*). Virions incorporating this mutant G are noninfectious and, when expressed on the cell surface, the mutant does not mediate cell–cell fusion (16). We incubated G_{th}, both wild-type (G_{th}-WT) and mutant (G_{th}-W72A), with liposomes at several pH values, separated the liposome-bound from free protein by sucrose-density centrifugation, and detected G_{th} in each fraction of the gradient by immunoblotting with a conformation-specific monoclonal antibody, IE2 (17).

At pH 8.0 and 7.4, most of the G_{th}-WT remained at the bottom of the gradient; at pH 6.6 and 6.0, most of it shifted to the top of the gradient, showing association ("coflotation") with the liposomes in that fraction (Fig. 4*B*). G_{th}-W72A did not associate with liposomes at any pH (Fig. 4*C*). The transition between pH 7.4 and 6.6 corresponds closely to the transition between rolling and arrest. Moreover, both transitions are reversible: Back-neutralization to pH 8.0 of G_{th}-WT incubated with liposomes at

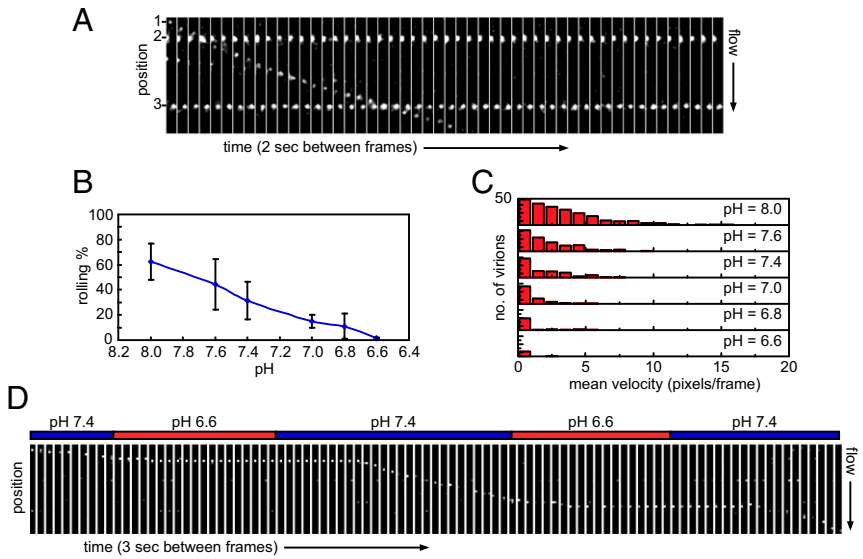

Fig. 3. VSV particles bind the target membrane in two modes. (*A*) Successive frames of a movie showing the two modes of binding at pH 7.4. Three particles are shown in white. Particles 2 and 3 are arrested and particle 1 rolls. Each frame is a 400-ms exposure taken every 2 s. The flow direction is down. (*B*) Percentage of VSV particles that are rolling at pH values between 8.0 and 6.6. Each point represents the average of three to four independent trials. Error bars show SD. (*C*) Distributions of mean velocities of rolling VSV particles at pH values between 8.0 and 6.6. Each bin represents the number of particles rolling with a mean velocity within the values indicated on the *x* axis. (*D*) Successive frames of a movie showing the reversibility of the transition between rolling and arrest. The particle is shown in white. The pH value at each time is indicated above the frames. Frames are 300-ms exposures taken every 3 s. The flow direction is down. The images shown in *A* and *D* have been sharpened with a Mexican hat filter and their contrast increased to aid in particle tracking.

pH 6.6 or 6.0 eliminated the coflotation (Fig. 4*D*), just as back-neutralization restored rolling. The failure of G_{th}-W72A to comigrate with liposomes on the gradient at any pH confirms that the properties of G_{th} probed in these experiments are indeed due to fusion-loop interactions with the lipid bilayer.

Discussion

Structural Interpretation of Hemifusion Kinetics. The soluble ectodomain, G_{th}, has the following conformational properties. At pH >7, it is in equilibrium between the "umbrella-like" prefusion trimer seen in crystals grown at elevated pH and an extended monomer. The interactions among subunits in the prefusion trimer are weak enough that the soluble ectodomain is monomeric at concentrations (~1 mg/mL) ordinarily used for biochemical characterization (18). At pH <7 and in the presence of a lipid bilayer (e.g., the liposomes in the experiments shown in Fig. 4), membrane binding through the fusion loops will favor trimer clustering and folding back into the inverted, postfusion conformation seen in crystals at acidic pH. Stable association with liposomes (and hence detectable coflotation) probably requires the joint participation of all three subunits. The conformational change and liposome binding are nonetheless reversible upon reneutralization (Fig. 4*D*), and the individual extended monomers can dissociate from the liposome; at suitable concentrations, they will also reform the soluble, prefusion trimer. Soluble forms of flavivirus E proteins show a similar, liposome-catalyzed trimerization, but in that case an irreversible one (19).

On the surface of a virion at neutral pH and above, our results together with published data indicate that full-length G is in equilibrium between the prefusion trimer conformation and flexibly extended monomers (10, 20–22). In the absence of a target membrane, irreversible transition of virion G to its conformation at the end of a complete fusion reaction would require that three subunits come together, fold back, and insert their fusion loops into the viral membrane (Fig. 1). There is a barrier to this transition even at pH 6.6, however, because exposure to that pH does not inactivate the virus (and because, in the presence of a target membrane, progression to hemifusion and fusion is immeasurably slow). Proton binding at pH ~6.4 and below

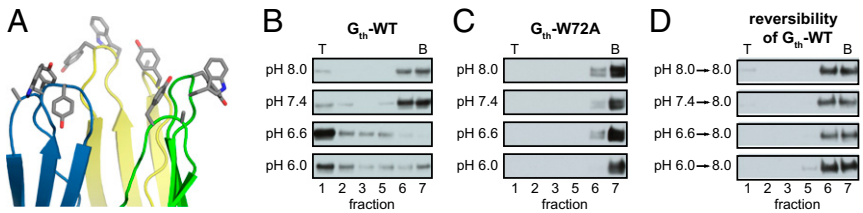

Fig. 4. Liposome interaction of a G fusion-loop mutant. (*A*) Close-up view of conserved hydrophobic residues at the tips of each fusion loop in a G trimer. Each G monomer is colored differently. The conserved hydrophobic residues—W72, Y73, Y116, and A117—are shown as sticks [PDB ID code 5I2M (11)]. (*B* and *C*) Cleaved ectodomain (G_{th}) from G-WT (*B*) or the fusion-loop mutant, G-W72A (*C*), was incubated with liposomes at the listed pH values. The mixtures were then separated over a discontinuous sucrose gradient, and each fraction was immunoblotted with the monoclonal antibody IE2 to detect the presence of G_{th}. Fraction numbers are along the bottom of each figure; the top (T) and bottom (B) fractions are also labeled. (*D*) In the reversibility experiment, G_{th}-WT was initially incubated with liposomes at the indicated starting pH before the pH was shifted to 8.0. After further incubation at pH 8.0, the mixtures were separated over a discontinuous sucrose gradient, also at pH 8.0.

lowers this barrier enough to allow the transition and to induce fusion when a target bilayer is present.

In view of the structural properties just summarized, we interpret the data in Figs. 2 and 3 as follows. (*i*) The equilibrium between prefusion trimer and extended monomer exposes the fusion loops and allows attachment of the virus to the supported bilayer, even in the absence of a specific receptor. At pH 8, the number of exposed loops is relatively sparse, and hydrodynamic drag can move the particle on the bilayer surface, either literally by rolling or by dragging along small patches of interacting lipid. As the pH decreases, attachment becomes progressively tighter (Fig. 3 *B* and *C*). The fusion loops of an extended monomer can withdraw from the membrane, as shown both by restoration of rolling after raising the pH and by reversibility of G_{th}–liposome association. The transition from prefusion trimer to extended monomer is not cooperative across the virion surface, as the pH dependence of the rolling–arrest equilibrium is gradual. (*ii*) Lowering the pH below 6.6 facilitates a further conformational change that allows the domains displaying the fusion loops to cluster as trimers and the C-terminal elements to zip back along the outside of this cluster. This transition will pull the two membranes together, provided that a critical number of adjacent postfusion trimers can form within the contact zone between virion and target membrane. Otherwise, the resistance of the two membranes to deformation will resist collapse. (*iii*) At the initial pH, the position of the equilibrium between prefusion trimer and extended monomer requires that after a drop to pH ≤6.2, some prefusion trimers must dissociate and monomers extend before a critical number of adjacent postfusion trimers will be present within the contact zone. A sequence of rate-limiting steps therefore intervenes between pH drop and collapse toward hemifusion, as shown by the nonexponential shape of the hemifusion delay time distributions in Fig. 2 *D–F*, *Top*. (Even at an initial pH of 6.6, the shape of the distribution in Fig. 2*F*, *Top*, deviates from exponential, although the rise and fall evident at the higher pH values are not detectable at the sampling interval allowed by 1,091 fusion events.) When the final pH is 5.5, the initial step (monomer extension) appears to be so rapid that the probability of forming a critical number of adjacent postfusion trimers within the contact zone is high, and cooperative collapse of those trimers becomes the sole rate-limiting event (Fig. 2 *D* and *E*, *Bottom*; with essentially single-exponential distributions).

Simulation of Hemifusion Kinetics. Based on the qualitative description above—(*i*) a reversible pH-dependent conformational change of the G protein, (*ii*) reversible G trimerization and clustering of fusion loops, and (*iii*) establishment of a critical number of adjacent "collapsible" trimers within the contact zone that can lead to irreversible hemifusion—we formulated a quantitative kinetic model (Fig. 5*A*, Table 1, and *Materials and Methods*). After parameter optimization, we can fit the experimental data with simulated hemifusion distributions calculated for the nine initial-to-final pH conditions (Fig. 5*B*).

Previous studies and data presented here show pH-dependent conformational changes in G and membrane association above pH 6.6 but a fusion threshold of pH 6.2. Whereas a pH-dependent conformational change in G is explicitly accounted for by pK_{a1} in our model (**1.1**), the "gating" of hemifusion at a lower pH can be explained by a combination of both a trimerization equilibrium of extended G molecules and the probability of forming a cluster of adjacent extended trimers. In other viruses such as influenza virus and West Nile virus, formation of the extended trimer is irreversible. The pH threshold for this step is essentially the pH threshold for fusion; below that threshold, the size of the critical cluster [and, in the case of influenza, the frequency of abortive transitions (23)] determines the fusion rate. With VSV G, for which formation of the extended trimer is reversible, the effective pH threshold for fusion is a convolution of effects due to the pH dependence of extended trimer formation and the critical cluster size.

The simulation suggests that four extended trimers in a cluster are sufficient to catalyze VSV fusion (Fig. S2). The corresponding numbers for influenza virus are between three, for subtype H3 (7), and five, for subtype H1 (23); for West Nile virus, the critical cluster appears to be just two trimers (5). Ensemble measurements on the rate of HIV fusion suggest that just one or two active envelope trimers may be sufficient to generate a fusion event (24), consistent with the relatively small number of spikes on a virion. Depending on details of structure and fusion-loop (or fusion-peptide) geometry, no more than about five or six trimers could fit around a hemifusion stalk or a nascent fusion pore having the dimensions shown by electron cryotomography of fusing influenza virus particles (25). Thus, the numbers derived from kinetic data are consistent with the geometry of the underlying molecular rearrangements.

Despite substantial molecular structural differences, the mechanisms for catalysis of fusion by influenza virus HA, West Nile virus E, and VSV G are essentially the same. In all three cases, proton binding is the trigger that initiates conformational transitions in the individual fusion-protein oligomers. Receptor or coreceptor binding is the corresponding trigger for viruses, such as paramyxoviruses and HIV, that fuse at neutral pH, but we expect that the ensuing process will follow a mechanism similar to the one we have described for those triggered by low pH.

Materials and Methods

Buffer Solutions. Buffers used for virus purification were HNE-10 pH 8.0 (10 mM Hepes, pH 8.0, 140 mM NaCl, 0.1 mM EDTA) and HNE-10 pH 7.4 (10 mM Hepes, pH 7.4, 140 mM NaCl, 0.1 mM EDTA).

In the hemifusion experiments, buffers at the initial pH values contained either 50 mM Hepes or 50 mM MES and buffers at the final pH values contained 100 mM MES. The increase in buffer concentration sharpened the transition from the initial pH to the final pH during the experiment. The sodium chloride concentration in these buffers was adjusted such that the total ionic strength of the buffer was ~150 mM. Ionic strength was calculated using the formula given in ref. 26. The initial pH buffers used were HNE-50 pH 8.0 (50 mM Hepes, pH 8.0, 130 mM NaCl, 0.1 mM EDTA), HNE-50 pH 7.4 (50 mM Hepes, pH 7.4, 140 mM NaCl, 0.1 mM EDTA), and MES-50 pH 6.6 (50 mM MES, pH 6.6, 130 mM NaCl, 0.1 mM EDTA). The final pH buffers used were MES-100 pH 6.2 (100 mM MES, pH 6.2, 122 mM NaCl, 0.1 mM EDTA), MES-100 pH 6.0 (100 mM MES, pH 6.0, 128 mM NaCl, 0.1 mM EDTA), and MES-100 pH 5.5 (100 mM MES, pH 5.5, 140 mM NaCl, 0.1 mM EDTA).

In the rolling experiments, the buffers used were HNE-50 pH 8.0 (50 mM Hepes, pH 8.0, 130 mM NaCl, 0.1 mM EDTA), HNE-50 pH 7.6 (50 mM Hepes, pH 7.6, 137 mM NaCl, 0.1 mM EDTA), HNE-50 pH 7.4 (50 mM Hepes, pH 7.4, 140 mM NaCl, 0.1 mM EDTA), HNE-50 pH 7.0 (50 mM Hepes, pH 7.0, 145 mM NaCl, 0.1 mM EDTA), MES-100 pH 6.8 (100 mM MES, pH 6.8, 108 mM NaCl, 0.1 mM EDTA), and MES-100 pH 6.6 (100 mM MES, pH 6.6, 112 mM NaCl, 0.1 mM EDTA).

All buffers used in imaging experiments were supplemented with 1 mM $CaCl_2$, 1 mM $MgCl_2$, and an oxygen-scavenging system composed of protocatechuate 3,4-dioxygenase from *Pseudomonas* (PCD; Sigma-Aldrich), 3,4-dihydroxybenzoic acid (protocatechuic acid; PCA; Sigma-Aldrich), and (±)-6-hydroxy-2,5,7,8-tetramethylchromane-2-carboxylic acid (Trolox; Sigma-Aldrich) at final concentrations of 100 nM, 2.5 mM, and 1 mM, respectively. The components of the oxygen-scavenging system were prepared as described (27).

Cells. BSR-T7 cells (28) and Vero cells (ATCC) were grown at 37 °C in Dulbecco's modified Eagle medium (DMEM; GIBCO) supplemented with 10% (vol/vol) FBS (GIBCO).

Virus Growth and Purification. Recombinant vesicular stomatitis virus (rVSV) was propagated in BSR-T7 cells and purified as follows (29). BSR-T7 cell monolayers were inoculated with rVSV (multiplicity of infection of 0.1) in DMEM supplemented with 2% (vol/vol) FBS and the antibiotics penicillin, streptomycin, and kanamycin for 18 to 20 h at 34 °C. After a low-speed centrifugation step to clear cell debris (2,000 × *g* for 5 min), virus particles were pelleted from the medium of infected cells by ultracentrifugation at 17,000 rpm for 1.5 h at 4 °C in an SW28 rotor (Beckman Coulter) and resuspended in

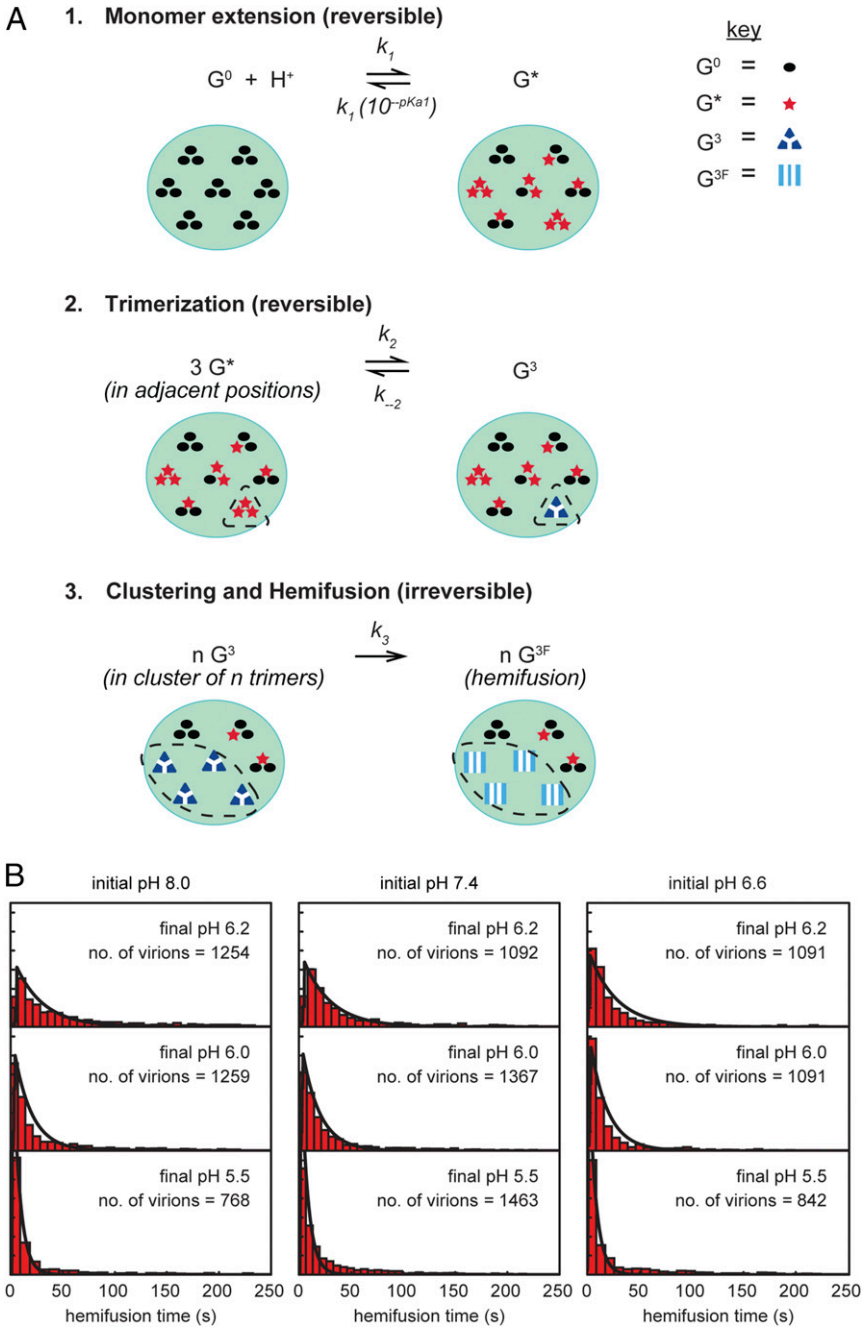

Fig. 5. Kinetic model for VSV fusion. (*A1*) Monomer extension (reversible). On the virion surface, we assume that G forms loosely associated prefusion trimers, in which each monomer is in the prefusion form G^0. Each G^0 monomer can protonate independently and extend reversibly to form extended monomer, G*, exposing the fusion loops. The relative concentrations of G^0 and G* at equilibrium are determined by the pH and an apparent pK_{a1}. The forward rate constant for extension is k_1, and the reverse rate constant is k_{-1} or $k_1(10^{-pKa1})$. (*A2*) Trimerization (reversible). Three adjacent extended G* monomers reversibly associate to form an extended trimer, G^3. The forward and reverse rate constants of this trimerization are k_2 and k_{-2}, respectively. To simplify the model, we assume that G* only trimerizes with its original prefusion trimer neighbors. (*A3*) Hemifusion (irreversible). A cluster of extended G^3 trimers folds back to mediate hemifusion. The number of trimers required to form the fold-back cluster is n. The irreversible fold-back step proceeds with rate constant k_3. In this diagram, a cluster of size $n = 4$ is shown. G proteins elsewhere in the particle can independently adopt any of the previously described conformations of G. (*B*) Fits of the model to experimental data (see also *Materials and Methods*). Shown here is the best fit (black line) obtained for patch size $P = 55$ trimers and fold-back cluster size $n = 4$, where $pK_{a1} = 7.1$, $k_1 = 9.1 \times 10^5$ $mol^{-1} \cdot L \cdot s^{-1}$, $k_2 = 2.0$ s^{-1}, $k_{-2} = 9.9$ s^{-1}, and $k_3 = 5.8$ s^{-1}. Experimental data (red bars) are from Fig. 2 *D–F*.

either HNE-10 pH 8.0 or HNE-10 pH 7.4 (*Buffer Solutions*) overnight at 4 °C. The concentrated virus suspension was further separated on a linear 15 to 45% (wt/vol) sucrose gradient formed in either HNE-10 pH 8.0 or HNE-10 pH 7.4 at 25,000 rpm for 3.5 h at 4 °C in an SW41 rotor (Beckman Coulter). The bottom band of virus particles was harvested by side puncture and concentrated by centrifugation through a 10% (wt/vol) sucrose cushion in either HNE-10 pH 8.0 or HNE-10 pH 7.4 at 33,000 rpm for 1 h at 4 °C in an SW50.1 rotor (Beckman Coulter). The virus pellet was resuspended in either HNE-10 pH 8.0 or HNE-10 pH 7.4 overnight at 4 °C. Purity and protein content of the virus particles were determined by SDS-PAGE and Coomassie staining. Viral titers were measured on monolayers of Vero cells as previously described (30).

Table 1. Reactions and equations for the kinetic model and simulations

Reactions

$$G^0 + H^+ \underset{k_{-1}}{\overset{k_1}{\rightleftarrows}} G^* \quad [1.1]$$

$$3\,(G^*)_{\text{in trimer}} = preG^3 \underset{k_{-2}}{\overset{k_2}{\rightleftarrows}} G^3 \quad [1.2]$$

$$n\,(G^3)_{\text{in cluster}} \xrightarrow{k_3} n\,(G^{3F})\ (\textit{hemifused virion}) \quad [1.3]$$

Kinetic differential equations

$$\frac{d[G^0]}{dt} = -k_1[G^0][H^+] + k_{-1}\,[G^*] \quad [2.1]$$

$$\frac{d[G^*]}{dt} = k_1[G^0][H^+] - k_{-1}[G^*] - 3k_2[preG^3] + 3k_{-2}[G^3] \quad [2.2]$$

$$\frac{d[G^3]}{dt} = k_2[preG^3] - k_{-2}[G^3] \quad [2.3]$$

$$\frac{dV_F}{dt} = \sum_{i=0}^{C_{\max}} \Pr_{n,P}(i\ \textit{clusters} \mid T)\cdot i \cdot k_3 \cdot (V_{\text{total}} - V_F), \quad [2.4]$$

where n is cluster size (number of adjacent G^3 trimers required for hemifusion), P is patch size, $C_{\max}$ is maximum number of clusters, T is number of G^3 trimers, V_{total} is total number of virions in the simulation, and V_F is number of fused virions.

Additional equations

$$k_{-1} = k_1 10^{-pKa_1} \quad [3.1]$$

$$[preG^3] = 0.622e^{-\left(\frac{\frac{[G^*]+3[G^3]}{[G]_{\text{total}}} - 1.458}{0.5783}\right)^2}([G^*] + 3[G^3]) - [G^3] \quad [3.2]$$

$$pH(t) = pH_{\text{final}} + \frac{pH_{\text{initial}} - pH_{\text{final}}}{e^{\frac{t-t_0}{0.75\ s}} + 1} \quad [3.3]$$

$$[H^+] = 10^{-\text{pH}} \quad [3.4]$$

$$T = round\left(\frac{3[G^3]}{[G]_{\text{total}}}P\right) \quad [3.5]$$

Virus Labeling. The total protein concentration of purified VSV was determined by Bradford assay (Bio-Rad) using a BSA standard. To label the viruses with lipophilic dye, 50 to 100 μL purified VSV (1 mg/mL in HNE-50 pH 8.0 or HNE-50 pH 7.4) was mixed with 0.5 to 1 μL octadecyl rhodamine B chloride (R18; 2 mM in ethanol; Invitrogen) for a final R18 concentration of 20 μM and incubated at room temperature (RT) for 1.5 to 2 h. The labeled virus was separated from unincorporated dye over a gel-filtration column (PD-10 desalting column or PD MidiTrap G-25 desalting column; GE Healthcare). There was less dilution of the labeled virus fraction when using the PD MidiTrap G-25 desalting column.

Flow-Cell Construction. Glass microscope coverslips (25 × 25 mm; no. 1.0; VWR) were cleaned by serial rounds of sonication in 7X-O-Matic detergent (VWR), 1 M potassium hydroxide, HPLC-grade acetone, and HPLC-grade ethanol for 10 to 20 min each round. The glass coverslips were thoroughly rinsed in Milli-Q water (Millipore) after each round of sonication. After the final sonication in ethanol, the coverslips were dried by baking at 110 °C. To render the surface of the glass hydrophilic, the coverslips were cleaned with oxygen plasma (0.5 torr) for 3 min (plasma etcher; March Plasmod). The flow cell was constructed by placing a polydimethylsiloxane (PDMS) device containing microfluidic channels (70 μm high × 0.5 mm wide × ∼5 mm long) onto a cleaned coverslip and sealing by compression. Inlet and outlet tubing was connected through holes bored in the PDMS device. To minimize the dead volume, inlet tubing with an inner diameter of 200 μm (Teflon FEP tubing; IDEX Health & Science) and a length of 6 cm was used. The outlet tubing (PE60 tubing, inner diameter 0.38 mm; BD Biosciences) was connected to a syringe pump (Harvard Apparatus), and flow was established by negative pressure across the channel.

Lipid Bilayer Preparation. Liposomes composed of cholesterol (Avanti Polar Lipids), 1,2-dioleoyl-*sn*-glycero-3-phosphocholine (DOPC; Avanti Polar Lipids), 1-palmitoyl-2-oleoyl-*sn*-glycero-3-phosphocholine (POPC; Avanti Polar Lipids), 1-palmitoyl-2-oleoyl-*sn*-glycero-3-phosphoethanolamine (POPE; Avanti Polar Lipids), disialoganglioside GD_{1a} from bovine brain (Sigma-Aldrich), and *N*-(fluorescein-5-thiocarbamoyl)-1,2-dihexadecanoyl-*sn*-glycero-3-phosphoethanolamine, triethylammonium salt (fluorescein DHPE; Invitrogen) in a molar ratio of 20:20:20:40:1:6.4 × 10^{-3} were prepared as follows. Purified lipids dissolved in chloroform, with the exception of GD_{1a}, which was dissolved in a 1:1 chloroform:methanol mixture, were combined in the molar ratio listed above and dried to a film under an argon gas stream. The film was further dried under vacuum for 2 h. The film was then resuspended in HNE-50 pH 7.4 at 20 mg/mL by five freeze–thaw cycles in liquid nitrogen. The resuspended lipid solution was extruded 21 times at 40 °C through a polycarbonate membrane with a pore size of 0.2 μm (Whatman) to form liposomes. The liposomes were diluted fourfold in HNE-50 pH 7.4 and flowed into a flow-cell channel. The liposomes were incubated in the flow cell at RT for 10 to 30 min, during which time they adsorbed to the glass, fused with neighboring liposomes, and ruptured to form a supported lipid bilayer on the glass coverslip.

Imaging Single-Particle Hemifusion. Labeled virus was diluted 50-fold in HNE-50 pH 8.0 or HNE-50 pH 7.4 and flowed at a rate of 0.04 mL/min into a flow cell containing a supported lipid bilayer until the desired density of virus on the bilayer was achieved. For experiments with an initial pH value of 6.6, labeled virus in HNE-50 pH 7.4 was flowed into the flow cell and then washed and incubated in HNE-50 pH 6.6 for 5 to 10 min. To initiate hemifusion, low-pH buffer was continuously flowed into the flow cell at a rate of 0.06 mL/min. The flow-cell channel was illuminated in TIRF mode simultaneously with a 488-nm solid-state laser (Coherent) and a 561-nm solid-state laser (Coherent) through an oil-immersion, high-numerical-aperture objective (N.A. 1.45). Fluorescence emission was collected through the same objective, filtered through a dual-band-pass filter (Chroma Technology), and recorded by an EMCCD camera (Hamamatsu ImagEM) at a frame rate of 5 Hz for 250 to 300 s. Laser powers of 40 μW for the 488-nm line and 5 μW for the 561-nm line, as measured on the laser table, were used. Transmittance through the objective was 53% for the 488-nm line and 56% for the 561-nm line. All experiments were conducted at room temperature.

Imaging Single-Particle Rolling. Labeled virus was diluted 50-fold in HNE-50 pH 8.0 and flowed at a rate of 0.04 mL/min into a flow cell containing a supported lipid bilayer until the desired density of virus on the bilayer was achieved. To image rolling at pH 8.0, HNE-50 pH 8.0 was continuously flowed into the flow cell at a rate of 0.06 mL/min. The flow-cell channel was illuminated in TIRF mode, and fluorescence emission was recorded as in the hemifusion observations above at a frame rate of 2.5 Hz for 100 to 200 s (lasers from Coherent; Andor iXon EMCCD camera). The buffer in the flow channel was then exchanged with HNE-50 pH 7.6, and the virus was incubated for 5 to 10 min in the new buffer before beginning imaging of rolling in pH 7.6 buffer under continuous flow. This buffer-exchange procedure was repeated for the remaining pH points of 7.4, 7.0, 6.8, and 6.6. At each pH point, a new upstream field of view was chosen to minimize light damage to the labeled VSV particles. Laser powers of 30 μW for the 488-nm line and 5 μW for the 561-nm line, as measured on the laser table, were used. Transmittance through the objective was 31% for the 488-nm line and 34% for the 561-nm line. All experiments were conducted at room temperature.

Data Analysis. The single-particle hemifusion data were analyzed as previously described (6). To analyze the single-particle rolling data, images were sharpened by convolution with a Mexican hat filter and smoothed by a median filter (pixel size of 2) using ImageJ software (NIH). Particle locations were picked manually in the first frame of the recorded movie. A rectangular region of interest (ROI) was defined for each particle in each frame of the movie, extending in the direction of flow from the initial particle location in the first frame to the edge of the field of view. These ROIs were used to construct position-versus-time kymographs for each particle, and the particle track was traced manually. Particle velocities were determined from the slopes of the traced particle tracks. The kymograph and velocity analyses were performed using custom-written software in MATLAB (MathWorks).

Negative-Stain Electron Microscopy. VSV particles were incubated in buffers HNE-50 pH 7.6, HNE-50 pH 7.0, and MES-50 pH 6.6 for at least 15 min at room temperature at a particle concentration of 0.05 to 0.1 mg/mL. The samples were adsorbed to carbon-coated collodion-support grids for 30 s, blotted, rinsed once in 2% (wt/vol) phosphotungstic acid (PTA), blotted, stained for 15 to 30 s with 2% (wt/vol) PTA, blotted again, and dried under light vacuum. The grids were glow-discharged before sample adsorption. The pH of the phosphotungstic acid was adjusted with sodium hydroxide to match the pH of the incubating buffer. Samples were examined using a JEOL 1200EX electron microscope operated at 80 kV (Department of Cell Biology Electron Microscopy

Facility, Harvard Medical School). The mean thickness of the G-protein layer and the SD are reported in *Results*.

G_{th} Purification. G_{th} was cleaved and purified from virus particles as described in ref. 21 with the following modifications. In the cleavage reaction, the concentration of WT virus was 10 mg/mL, of G-W72A virus 11.1 mg/mL, and of thermolysin 0.6 mg/mL. Virus concentration was measured by Bradford assay (Bio-Rad) using a BSA standard curve. Total reaction volumes ranged from 300 to 700 μL. Proteolysis was stopped by the addition of both blocking buffer (900 mM Tris·HCl, pH 8.8, 50 mM EDTA) and protease inhibitor mixture (cOmplete, EDTA-free; Roche). Cleavage reactions were then spun through 20% (wt/vol) sucrose cushions [20% (wt/vol) sucrose, 20 mM Tris·HCl, pH 8.8, 10 mM EDTA] in a TLS-55 rotor (Beckman Coulter) at 48,000 rpm for 1 h at 4 °C. Supernatants were diluted 1:10 in buffer A (10 mM Tris·HCl, pH 8.8, 10 mM EDTA) and loaded onto an anion-exchange column (HiTrap Q HP 5-mL column; GE Healthcare). G_{th} was eluted with a linear gradient of buffer B (10 mM Tris·HCl, pH 8.8, 1 M NaCl, 10 mM EDTA); G_{th} eluted at ∼21 to 23% buffer B. Purified G_{th} was concentrated through an Amicon Ultra-4 centrifugal filter unit with a 10-kDa molecular-weight cutoff (Millipore). Final G_{th} concentration was determined by densitometry of Coomassie-stained gels using a BSA standard curve. Purified G_{th} was stored at 4 °C and used within 3 to 4 d for liposome-flotation experiments.

Liposome Association of G_{th}. The liposome-association assay was modified from a previously described protocol (31). Liposomes were prepared as described in the previous section but resuspended at a concentration of 10 mg/mL in HNE-50 pH 8.0, HNE-50 pH 7.6, MES-100 pH 6.6, and MES-100 pH 6.0 buffers. All solutions used in the liposome-association assay, including the liposomes and the sucrose-gradient solutions, were supplemented with EDTA such that the final EDTA concentration was 5 mM. Five microliters of either G_{th}-WT (0.53 μg/μL) or G_{th}-W72A (0.52 μg/μL) was mixed with 20 μL liposomes and 125 μL of the matching pH buffer for a total reaction volume of 150 μL. The reactions were incubated on a Labquake for 1 h at 37 °C. The reactions were then mixed thoroughly with 200 μL of 70% (wt/vol) sucrose solution to yield a final sucrose concentration of 40% (wt/vol). To form a discontinuous sucrose gradient, the association reaction in 40% (wt/vol) sucrose was placed at the bottom of a centrifuge tube. Nine hundred microliters of 25% (wt/vol) sucrose solution was layered on top and 150 μL of 5% (wt/vol) sucrose solution was layered on top of that. Each sucrose solution was made in the pH buffer matching that of the association reaction (i.e., HNE-50 pH 8.0, HNE-50 pH 7.6, MES-100 pH 6.6, or MES-100 pH 6.0 buffer). The gradients were spun in a TLS-55 rotor at 52,000 rpm for 2.5 h at 4 °C. Two-hundred-microliter fractions were collected from the top of the gradient using wide-bore pipette tips. The fractions were stored at 4 °C before SDS-PAGE and immunoblotting.

In the case of the reversible-reaction samples, the initial association was done in a reaction volume of 100 μL (5 μL G_{th}-WT + 20 μL liposomes + 75 μL matching pH buffer). After the 1-h incubation at 37 °C, 50 μL of 1 M Hepes (pH 8.0) was added to each reaction to raise the pH to 8.0 and the reactions were incubated for another 1 h at 37 °C. The sucrose gradients were prepared as described above, but only the pH 8.0 sucrose solutions were used.

Western Blotting for G_{th}. Fraction samples were heated at 95 °C in nonreducing sample buffer, separated by 4 to 20% (wt/vol) SDS-PAGE (Criterion TGX precast gels; Bio-Rad) under nonreducing conditions, and transferred to polyvinylidene fluoride membranes. G_{th} was detected with the monoclonal antibody IE2 at a 1:4 dilution, followed by a horseradish peroxidase-conjugated goat anti-mouse IgG. Western blots were developed using a chemiluminescent peroxidase substrate (SuperSignal West Pico Chemiluminescent Substrate; Thermo Scientific) and exposure to film.

Kinetic Model and Simulations. In our kinetic model for membrane fusion mediated by VSV G (Fig. 5 and Table 1), the G protein can adopt or participate in four distinct conformations or species. These are as follows: G^0, an unprotonated G monomer in prefusion conformation; G*, a protonated extended G monomer; G^3, a trimer of extended G protein; and G^{3F}, a trimer of G in its postfusion conformation.

The first reaction is reversible protonation and a conformational change of G^0 to G* with apparent pK_{a1} (Fig. 5*A1* and reaction **1.1**), where pK_{a1} is defined by the forward and reverse rate constants (Eq. **3.1**). The second reaction is reversible trimerization of $preG^3$ (three monomeric but adjacent G* molecules) to form a G^3 trimer (Fig. 5*A2* and reaction **1.2**). We calculate the concentration of $preG^3$ with Eq. **3.2**. To trimerize, three G* monomers must be adjacent to each other on the surface of the virus. Therefore, the concentration of $preG^3$ depends both on the concentration of G* and on the probability that the G* molecules are in the correct geometry to trimerize. We used a Monte Carlo simulation (implemented in MATLAB) to determine the probability that G* would be in a geometry allowing trimerization. We constructed patches containing m monomers of G (where m equals three times the patch size P on the surface of the virion), seeded the patch with different numbers of G* monomers, ranging from 0 to m, and counted the number of trimers on each patch. We assumed that each G* monomer is potentially a member of only one trimer. We simulated 500 patches for each seed value of G* and calculated the probability that G* could trimerize for that seed value of G*. We fit a Gaussian function to our simulated probabilities to obtain the probability distribution for $preG^3$ given the concentration of G*. We found that the probability distributions converged for patch sizes greater than 30 monomers. Eq. **3.2** is a Gaussian fit to the converged distribution for the concentration of $preG^3$ (Fig. S3). The final and third reaction is irreversible hemifusion requiring a concerted conformational change of a cluster of n extended G^3 trimers within a patch on the surface of the virion (Fig. 5*A3* and reaction **1.3**).

Based on these reactions, the kinetic differential equations describing the time-dependent changes of each of these G species are also shown in Table 1 (Eqs. **2.1**–**2.4**). The pH in the system was modeled as a sigmoidal curve, where the pH dropped from $pH_{initial}$ to pH_{final} at $t_0 = 600$ s, over a period of ∼3.0 s (4×0.75 s) (Eq. **3.3**). We chose a sigmoidal curve over a sharp step function for better numerical integration of the differential equations (see below). Eq. **3.4** relates pH and $[H^+]$. Whereas $[G^0]$, $[H^+]$, [G*], $[preG^3]$, and $[G^3]$ are local concentrations of the species on the virion surface in mol·L^{-1}, T is the number of G^3 trimers in a patch with size P, and V_{total} and V_F are the numbers of total and fused virions, respectively. We used Eq. **3.5** to calculate T from $[G^3]$, where P is the maximal number of trimers for a given patch size. In a population of virions, however, different virions may be able to form different numbers of G^3 clusters, and virions with more G^3 clusters will have a higher probability of hemifusing than virions with fewer G^3 clusters. Therefore, over a population of virions, the rate of hemifusion is the weighted sum of the individual fusion rates of virions containing different numbers of clusters, from 0 to C_{max}, where the weights are the probabilities that a virion contains i clusters at a given number T, which is $Pr_{n,P}(i \text{ clusters} \mid T)$ in Eq. **2.4**. To find these probabilities, we again used Monte Carlo simulations (implemented in MATLAB). We simulated the virion as a roughly circular patch of P points on a hexagonal array for $P = 13$, 31, 55, 73, and 109. Each point represented the position of a potential G^3 trimer on the virion surface. For a given $[G^3]$, we calculated the number of G^3 trimers that would correspond to on the patch and simulated 10,000 virions in which that number of points on the patch were randomly assigned a G^3 conformation. Clusters of adjacent G^3 trimers were then detected on each simulated virion. We defined clusters of three, four, five, and six adjacent G^3 trimers ($n = 3$, 4, 5, or 6) as previously outlined in ref. 7. The numbers of simulated virions containing 0 to C_{max} clusters were tallied separately and divided by the total number of virions to obtain the probabilities. For computational efficiency, the probabilities were calculated for all possible T for a given patch size and stored as matrices, where each row represented a given T and each column was the probability of forming i clusters at that concentration.

We numerically integrated the differential equations using the odeint function implemented in the SciPy Python library (version 0.17.0) (https://www.scipy.org). The goal of model optimization is to find the set of parameter values that gives the best fit of the model to the observed data. We measured the quality of fit by calculating the root-mean-square deviation (rmsd) between the numbers of fused viruses at each time point in the model and experiment. We globally matched all nine regimes of initial and final pH simultaneously. Finding the global minimum of the multidimensional model function is nontrivial, and we therefore used a two-step approach. First, we ran simulations for a grid of parameter values, which explored five or six values for each parameter in the following range: $pK_{a1} = 6.5$ to 7.3, $k_1 = 100$ to 800,000 $mol^{-1}{\cdot}L{\cdot}s^{-1}$, $k_2 = 0.01$ to 10 s^{-1}, $k_{-2} = 0.01$ to 10 s^{-1}, and $k_3 = 0.01$ to 5 s^{-1}; patch sizes of $P = 13$, 31, 55, 73, and 109; and cluster sizes of $n = 3$, 4, 5, and 6. In a second step, we further optimized the best fit of the initial grid search for each combination of P and n using the SciPy minimization function with the Nelder–Mead algorithm (32).

ACKNOWLEDGMENTS. We thank Anna Loveland and Joe Loparo for help with TIRF microscopy and discussions; Amy Lee and David Cureton for help with virus growth and purification; Erick Matsen and Kyung-Suk Kim for initial discussions on the model; Maria Ericsson and the Harvard Medical School Cell Biology Electron Microscopy Facility; and Raffaele Potami for help with setting up parallel computing. I.S.K. acknowledges a National Science Foundation Graduate Research Fellowship. The research was supported by NIH Grant CA-13202 to S.C.H., who is an Investigator in the Howard Hughes Medical Institute.

1. Chernomordik LV, Zimmerberg J, Kozlov MM (2006) Membranes of the world unite! *J Cell Biol* 175(2):201–207.
2. Leikin S, Parsegian VA, Rau DC, Rand RP (1993) Hydration forces. *Annu Rev Phys Chem* 44:369–395.
3. Harrison SC (2008) Viral membrane fusion. *Nat Struct Mol Biol* 15(7):690–698.
4. Harrison SC (2015) Viral membrane fusion. *Virology* 479–480:498–507.
5. Chao LH, Klein DE, Schmidt AG, Peña JM, Harrison SC (2014) Sequential conformational rearrangements in flavivirus membrane fusion. *eLife* 3:e04389.
6. Floyd DL, Ragains JR, Skehel JJ, Harrison SC, van Oijen AM (2008) Single-particle kinetics of influenza virus membrane fusion. *Proc Natl Acad Sci USA* 105(40): 15382–15387.
7. Ivanovic T, Choi JL, Whelan SP, van Oijen AM, Harrison SC (2013) Influenza-virus membrane fusion by cooperative fold-back of stochastically induced hemagglutinin intermediates. *eLife* 2:e00333.
8. Lyles DS, Rupprecht CE (2007) Rhabdoviridae. *Fields Virology*, eds Knipe D, Howley P (Lippincott Williams & Wilkins, Philadelphia), 5th Ed, Vol 1, pp 1363–1408.
9. Gaudin Y (2000) Reversibility in fusion protein conformational changes. The intriguing case of rhabdovirus-induced membrane fusion. *Subcell Biochem* 34:379–408.
10. Gaudin Y, Ruigrok RW, Knossow M, Flamand A (1993) Low-pH conformational changes of rabies virus glycoprotein and their role in membrane fusion. *J Virol* 67(3): 1365–1372.
11. Roche S, Bressanelli S, Rey FA, Gaudin Y (2006) Crystal structure of the low-pH form of the vesicular stomatitis virus glycoprotein G. *Science* 313(5784):187–191.
12. Roche S, Rey FA, Gaudin Y, Bessanelli S (2007) Structure of the prefusion form of the vesicular stomatitis virus glycoprotein G. *Science* 315(5813):843–848.
13. Roche S, Albertini AA, Lepault J, Bressanelli S, Gaudin Y (2008) Structures of vesicular stomatitis virus glycoprotein: Membrane fusion revisited. *Cell Mol Life Sci* 65(11): 1716–1728.
14. White J, Matlin K, Helenius A (1981) Cell fusion by Semliki Forest, influenza, and vesicular stomatitis viruses. *J Cell Biol* 89(3):674–679.
15. Libersou S, et al. (2010) Distinct structural rearrangements of the VSV glycoprotein drive membrane fusion. *J Cell Biol* 191(1):199–210.
16. Stanifer ML, Cureton DK, Whelan SP (2011) A recombinant vesicular stomatitis virus bearing a lethal mutation in the glycoprotein gene uncovers a second site suppressor that restores fusion. *J Virol* 85(16):8105–8115.
17. Lefrancois L, Lyles DS (1982) The interaction of antibody with the major surface glycoprotein of vesicular stomatitis virus. I. Analysis of neutralizing epitopes with monoclonal antibodies. *Virology* 121(1):157–167.
18. Doms RW, Keller DS, Helenius A, Balch WE (1987) Role for adenosine triphosphate in regulating the assembly and transport of vesicular stomatitis virus G protein trimers. *J Cell Biol* 105(5):1957–1969.
19. Stiasny K, Allison SL, Schalich J, Heinz FX (2002) Membrane interactions of the tick-borne encephalitis virus fusion protein E at low pH. *J Virol* 76(8):3784–3790.
20. Durrer P, Gaudin Y, Ruigrok RW, Graf R, Brunner J (1995) Photolabeling identifies a putative fusion domain in the envelope glycoprotein of rabies and vesicular stomatitis viruses. *J Biol Chem* 270(29):17575–17581.
21. Albertini AA, et al. (2012) Characterization of monomeric intermediates during VSV glycoprotein structural transition. *PLoS Pathog* 8(2):e1002556.
22. Ferlin A, Raux H, Baquero E, Lepault J, Gaudin Y (2014) Characterization of pH-sensitive molecular switches that trigger the structural transition of vesicular stomatitis virus glycoprotein from the postfusion state toward the prefusion state. *J Virol* 88(22): 13396–13409.
23. Ivanovic T, Harrison SC (2015) Distinct functional determinants of influenza hemagglutinin-mediated membrane fusion. *eLife* 4:e11009.
24. Yang X, Kurteva S, Ren X, Lee S, Sodroski J (2005) Stoichiometry of envelope glycoprotein trimers in the entry of human immunodeficiency virus type 1. *J Virol* 79(19): 12132–12147.
25. Calder LJ, Rosenthal PB (2016) Cryomicroscopy provides structural snapshots of influenza virus membrane fusion. *Nat Struct Mol Biol* 23(9):853–858.
26. Kochaniak AB, et al. (2009) Proliferating cell nuclear antigen uses two distinct modes to move along DNA. *J Biol Chem* 284(26):17700–17710.
27. Aitken CE, Marshall RA, Puglisi JD (2008) An oxygen scavenging system for improvement of dye stability in single-molecule fluorescence experiments. *Biophys J* 94(5):1826–1835.
28. Buchholz UJ, Finke S, Conzelmann KK (1999) Generation of bovine respiratory syncytial virus (BRSV) from cDNA: BRSV NS2 is not essential for virus replication in tissue culture, and the human RSV leader region acts as a functional BRSV genome promoter. *J Virol* 73(1):251–259.
29. Whelan SP, Ball LA, Barr JN, Wertz GT (1995) Efficient recovery of infectious vesicular stomatitis virus entirely from cDNA clones. *Proc Natl Acad Sci USA* 92(18):8388–8392.
30. Schott DH, Cureton DK, Whelan SP, Hunter CP (2005) An antiviral role for the RNA interference machinery in *Caenorhabditis elegans*. *Proc Natl Acad Sci USA* 102(51): 18420–18424.
31. Kim IS, Trask SD, Babyonyshev M, Dormitzer PR, Harrison SC (2010) Effect of mutations in VP5 hydrophobic loops on rotavirus cell entry. *J Virol* 84(12):6200–6207.
32. Nelder JA, Mead R (1965) A simplex method for function minimization. *Comput J* 7(4): 308–313.
33. Sun X, Belouzard S, Whittaker GR (2008) Molecular architecture of the bipartite fusion loops of vesicular stomatitis virus glycoprotein G, a class III viral fusion protein. *J Biol Chem* 283(10):6418–6427.
34. Carneiro FA, et al. (2003) Membrane fusion induced by vesicular stomatitis virus depends on histidine protonation. *J Biol Chem* 278(16):13789–13794.